

Quantitative measurement of grain boundary potentials on the nanoscale by off-axis electron holography

M. A. Schofield, L. Wu, and Y. Zhu

Department of Materials Science, Brookhaven National Laboratory, Upton, New York 11973

(Received 3 May 2002; revised manuscript received 19 August 2002; published 19 June 2003)

We explore the quantification of the grain boundary potential across *c*-axis aligned twist boundaries in $\text{Bi}_2\text{Sr}_2\text{CaCu}_2\text{O}_{8+\delta}$ superconductors using off-axis electron holography. In separating the bulk contribution to the potential profile we find that a kinematical treatment is sufficient to quantify the potential associated with only the grain boundary. We model the measured potential with a Gaussian function to determine the charge density across several boundaries as a function of the interface misorientation. We further examine the effect of objective lens aberration and defocus on the potential quantification for subnanometer resolution and conclude that it may be neglected for spatial resolution above 5 Å, which is suitable for the boundaries under study. We find no dependence of the measured potential or grain boundary width on the misorientation angle. We measure an average grain boundary potential of 2.18 ± 0.12 V corresponding to about a 8.6 Å interface width, and conclude that a negative charge of $1.7e^-$ /unit cell is associated with the grain boundary core. The treatment presented here has general validity for the quantitative study of interface potential.

DOI: 10.1103/PhysRevB.67.224512

PACS number(s): 74.72.Hs, 61.72.Mm, 61.14.Nm

I. INTRODUCTION

One of the most challenging tasks in solid-state physics and materials science research is to understand the electronic properties of interfaces. For example, the electronic transport properties of interfaces between metals, semiconductors, and insulators in semiconductor devices play an important role in determining the functionality of the device.¹ In polycrystalline high-temperature superconductors, e.g., $\text{YBa}_2\text{Cu}_3\text{O}_{7+\delta}$, grain boundaries (GB's) are often considered a source of transport resistance, where the critical current can be significantly lower than that of the grain interior for misorientation angles greater than 10° .²⁻⁵ This significantly hampers realization of the superconductors for commercial power applications.

Recent theory and experiment suggest several possible origins for such grain boundary behavior, ranging from GB defects such as dislocations and depletion of oxygen hole content due to interfacial strain,^{6,7} to the phase shift of the $d_{x^2-y^2}$ wave symmetry function across the boundary. In particular, it was reported recently that reducing the structure induced GB charge in $\text{YBa}_2\text{Cu}_3\text{O}_{7+\delta}$ by replacing some of the Y^{3+} ions by Ca^{2+} ions enhances the GB transport properties.^{8,9} All of these origins can be associated with bending of the electronic band structure at the interface, which leads to a change in the density of charge carries at the interface and the nearby grain interior. Therefore, being able to accurately measure, experimentally, the electrostatic potential across an interface with known geometry is of considerable desire. We set out to map the potential variation across GB's in the high-temperature superconductor $\text{Bi}_2\text{Sr}_2\text{CaCu}_2\text{O}_{8+\delta}$ (Bi/2212) using off-axis electron holography. Electron holography allows retrieval of both the phase and amplitude of the electron wave¹⁰ passing through the sample, and this is the primary advantage since the electron phase shift carries the information of electric and magnetic

fields in the sample. We chose to study (001) twist boundaries in *c*-axis aligned polycrystalline tapes as a first step for the following three reasons: First, Bi/2212 textured wires and tapes are the most promising forms of superconductors for practical large scale application, and (001) twist boundaries are the dominant boundaries present in these materials.¹¹ Secondly, benign and angular-independent transport properties of these boundaries have been observed by careful measurements made on high quality bulk bicrystals. That is to say, these boundaries do not act as weak links and carry current as their grain constituents,¹² which is not the usual case for other high- T_c superconductors.² Finally, the atomic structure of GB's generally depends on the exact boundary-plane normal. For example, tilt boundaries exhibit faceting and meandering, especially in films, where the arrangement of local interfacial defects often vary in extent and periodicity even for boundaries with the same geometry. In contrast, the atomic plane of the (001) twist boundary in Bi/2212 is well defined, being located in the middle of the BiO-BiO layer. The interface is atomically sharp and straight, and the out-of-plane strain and displacement is negligibly small based on atomic imaging and simulation.¹³ These characteristics make (001) twist boundaries in Bi/2212 an ideal model system for one-dimensional potential measurement where we can average the potential profile along the GB to obtain much improved statistics (signal-to-noise ratio) and derive meaningful values of physical quantities from the measurements. Such a model system also allows us to (1) optimize experimental and reconstruction procedures to obtain a minimum resolution required for the interface under study (in our case, 0.6 nm, or, $\frac{1}{5}$ of the unit cell length normal to the boundary), (2) remove the effect of thickness, and (3) separate the interface potential from the bulk contribution. The results presented here may provide a fingerprint for the intrinsic nature of negatively charged twist boundaries in Bi/2212 and hopefully stimulate study of the electrostatic potential at interfaces in general.

II. EXPERIMENTAL

The results of holography experiments presented here were carried out in a JEOL 3000-*F* field-emission TEM operated at 300 kV. Our microscope is equipped for electron holography with a retractable biprism assembly consisting of a platinum wire $<0.6 \mu\text{m}$ in diameter. The biprism wire is rotatable $\pm 90^\circ$ and located approximately in the selected area aperture plane of the microscope. The multiscan CCD camera located after the Gatan Image Filter (GIF) attached to the microscope was used to record holograms.¹⁴

Samples suitable for TEM were prepared by standard techniques of mechanical thinning and polishing, with final thinning using Ar ion beam at liquid N₂ temperature. The final Ar milling produced a small perforation around which the material was electron transparent, and samples were oriented during preparation so that the vast majority of grain boundaries ended up more or less perpendicular to the perforation edge. This provided the most favorable sample geometry for the holography experiments (where an adjacent sample edge is required) for the following two reasons: First, holograms could be recorded with significant regions of each grain present in the hologram. This allowed the “bulk” (or grain interior) contribution from each grain to be independently eliminated from the reconstructed phase, as discussed later, leaving only contributions from the grain boundary for further analysis. The second advantage was that higher quality holograms could be recorded if the grain boundary was oriented perpendicular to the sample edge. For an edge-on (001) twist boundary, each grain is in a systematic row orientation and Bragg diffraction occurs normal to the grain boundary. Since the orientation of the holographic fringes is roughly defined by the sample edge and a biprism bias is used to separate the sidebands from the autocorrelation, a lower biprism voltage is required for separation when the systematic row direction is parallel to the fringes. This results in better fringe contrast and higher quality reconstruction for a given resolution.

Before detailed studies, a large number of grain boundaries were surveyed in order to determine the optimum conditions with regard to field of view, spatial resolution and hologram quality for reliable reconstruction of the grain boundary potential. It was found that subnanometer resolution with high fringe contrast was required to obtain meaningful grain boundary data, implying small, narrow potential distributions associated with the interfaces under study. Using the free lens control mode of our microscope we were able to record holograms with about 30–35 nm field of view and 20–25 % fringe contrast in vacuum for 2 Å fringes. Under these conditions we can record holograms with a 2 s exposure having suitable detection quantum efficiency of the CCD camera,¹⁴ and mechanical stability of the sample stage and biprism assembly. The reasonably large field of view meant that about 5–8 half unit cells (where $d_{002} = 1.5 \text{ nm}$) of the grain interior on each side of the grain boundary were present in the holograms. This was sufficient to assess the bulk contribution to the potential distribution of the grain boundary region, as discussed in the next section, and address the issue of dynamical scattering effects on the mea-

sured GB potential. The final preliminary concern before detailed study of individual grain boundaries is that of spatial resolution in the reconstructed phase. Since holography formally allows reconstruction of the *image* wave (not *object* wave) one must consider the effect of objective lens transfer at the resolution being considered. In the following section we also address this issue.

III. QUANTIFICATION OF GRAIN BOUNDARY POTENTIAL

A. Spatial resolution

It is conventional to describe the objective lens aberration and defocus by multiplication of the object wave $\psi_{\text{object}}(q)$ in reciprocal space by a phase factor $\chi(q)$ such that the image wave¹⁵

$$\psi_{\text{image}}(q) = \psi_{\text{object}}(q) \exp[i\chi(q)]. \quad (1)$$

A faithful transfer of object-amplitude to image-amplitude and object-phase to image-phase occurs for $\chi(q)$ small. It is sufficient here to consider only the lowest order coherent lens aberrations with radial symmetry so that the phase factor

$$\chi(q) = \pi \lambda_e \Delta f q^2 + \frac{\pi}{2} C_s \lambda_e^3 q^4. \quad (2)$$

Here, Δf is the lens focus, λ_e the electron wavelength, and C_s the spherical aberration of the objective lens.

We note that Eq. (2) exhibits a global minimum for negative focus (i.e., defocused objective lens) at

$$q_0^2 = -\frac{\Delta f_0}{C_s \lambda_e^2}, \quad (3)$$

where Δf_0 is any given lens defocus. At q_0 , χ is negative and carries an absolute value, say χ_0 , so Eq. (2) gives

$$\Delta f_0 = -\sqrt{\frac{2\chi_0 C_s \lambda_e}{\pi}}. \quad (4)$$

Since $\chi(q)$ is monotonically increasing for $q > q_0$, $\exists q_{\text{max}}$ such that $|\chi| \leq \delta \forall q \leq q_{\text{max}}$. In particular, setting $\chi = +\chi_0$ and $\Delta f = \Delta f_0$ in Eq. (2),

$$q_{\text{max}}^2 = \sqrt{\frac{2\chi_0}{\pi C_s \lambda_e^3}} (1 + \sqrt{2}). \quad (5)$$

Returning to Eq. (1), the reconstructed image wave will be a faithful representation of the object wave if $\chi(q)$ is close enough to zero for some range of q . If one defines the minimum resolution $r_{\text{min}} \equiv 1/q_{\text{max}}$, obtainable for variations in the phase factor $|\chi| \leq +\chi_0$, then

$$r_{\text{min}} = \left(\frac{\pi C_s \lambda_e^3}{2\chi_0} \right)^{1/4} (1 + \sqrt{2})^{-1/2}. \quad (6)$$

Equation (6) gives the minimum resolution over which the phase factor deviates from zero by less than χ_0 , and gives the resolution to which the object and image waves are the same within this tolerance.

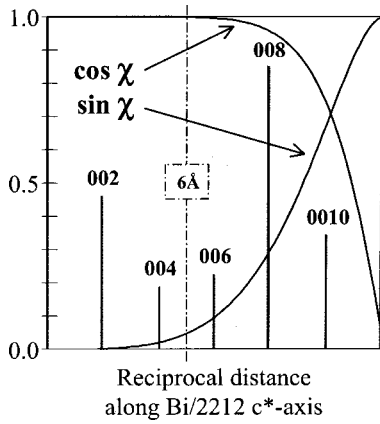


FIG. 1. Real and imaginary parts $\cos \chi$ and $\sin \chi$, respectively, of the objective lens transfer function plotted for zero defocus along the reciprocal c^* axis of Bi/2212. For resolution better than about 6 Å the objective lens aberration begins to affect the reconstructed amplitude and phase. Objective lens aberrations may be neglected for reconstruction with the aperture edge at the (forbidden) 005 Bragg reflection of Bi/2212.

For our microscope, $C_s = 0.55$ mm and $\lambda_e = 1.97$ pm at 300 keV. Hence, for small deviation less than say $\chi_0 = 0.1$ rad, $r_{\min} = 3.3$ Å. From Eq. (4) this corresponds to an objective lens defocus of 8.3 nm. Since the lens defocus is not precisely known in these experiments, we may also estimate the minimum resolution under the assumption $\Delta f = 0$. From Eq. (2) with $\chi = 0.1$ and $q = 1/r_{\min}$, we have $r_{\min} = 5.1$ Å. Hence, the lens defocus is not so critical as to limit meaningful quantification provided it is close enough (within ~ 10 nm here) to zero. These results are shown in Fig. 1, where the real and imaginary parts of $e^{i\chi}$ at $\Delta f = 0$ are plotted along the Bi/2212 reciprocal c axis (normal to the grain boundary). The figure shows that with regard to the Bragg reflections, reconstruction of the holograms at about 6 Å provides the best spatial resolution where the objective lens aberrations may be neglected.

B. Reconstruction and extraction of the GB potential

Figure 2(a) shows a typical hologram with a (001) twist boundary viewed edge on. The parallel pairs of thin dark lines in the hologram correspond to the BiO-BiO layers of the crystal with periodicity of 1.5 nm along the c axis. The fine 2 Å fringes running from the upper-left to lower-right of the hologram are the interference fringes that carry the desired phase information. Figure 2(b) is the corresponding diffractogram of the hologram shown in Fig. 2(a). Although in this case the grain boundary position is not ideal with respect to the biprism, i.e., the systematic row not being normal to the hologram fringes, the sidebands are well separated from the autocorrelation for the 6 Å numerical aperture (as indicated by the circle) used for reconstruction. The results of reconstruction are shown in Figs. 2(c) (amplitude) and 2(d) (phase). Artifacts at the edges of the reconstructed amplitude and phase are due to a Hanning window applied to the hologram that was necessary to reduce artifacts associated with the relatively small (Butterworth) aperture function used to

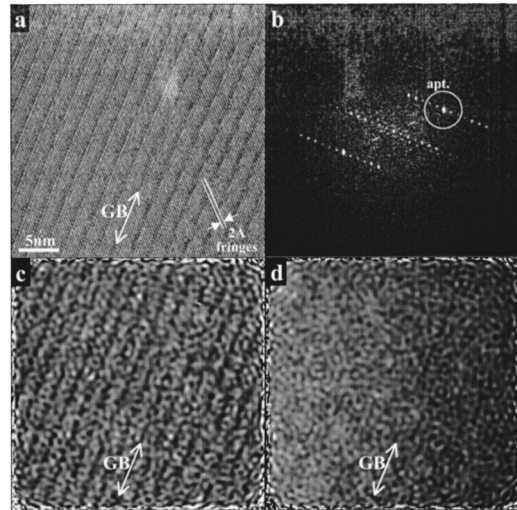


FIG. 2. (a) Typical hologram from Bi/2212 [001] twist boundary with 2 Å interference fringes. The BiO-BiO layers are visible parallel to the GB, indicating a nearly edge-on geometry. (b) Calculated diffractogram of the hologram in (a). The aperture (corresponding to 6 Å resolution) used to isolate the sideband for (c) amplitude and (d) phase reconstruction is indicated. The BiO-BiO layers are clearly visible in the reconstructed amplitude, while the GB may be discerned weakly in the phase image. Averaging the phase parallel to the interface improves the signal-to-noise ratio.

extract the sideband.¹¹ The BiO double layers are clearly visible in the amplitude image, while nearly invisible in the phase image. Nevertheless, the grain boundary can be discerned and subsequent averaging parallel to the interface improved the signal to noise.

For example, the estimated standard deviation to the measured phase shift¹⁶ corresponding to the experimental conditions and reconstruction in Fig. 2 is about $\pi/25$ rad. Averaging parallel to the interface improves the estimated measurement sensitivity to about $\pi/130$ rad. These values translate to a sensitivity in the measured potential, assuming a sample thickness of 10 nm, of about 2 V before averaging and 0.3 V afterwards. These estimates indicate that our experimental conditions are sufficiently sensitive to measure, for instance, a 2 V GB potential after averaging along the interface. As we see below, however, a main source of measurement error in determining the GB potential lies in estimating the contribution to the phase profile corresponding to the grain interior. Consequently, we recorded a number of holograms (usually 3) from the same grain boundary in order to further improve the signal to noise ratio and reduce systematic artifacts associated with the reconstruction.

Given an averaged phase profile across an interface $\phi(x)$ the simplest treatment to access the contribution to the phase shift due only to the GB is to write $\phi(x) = \phi_{\text{GB}}(x) + \phi_{\text{bulk}}(x)$, where $\phi_{\text{GB}}(x)$ and $\phi_{\text{bulk}}(x)$ are the GB and bulk contributions, respectively. In general, this prescription is valid if there is not a strong coupling of scattering between the GB and bulk, which can be done by keeping the crystal off any major zone axis. In our experiments we have tilted to a systematic row orientation to minimize multiple scattering while retaining an edge-on view of the GB. To address the

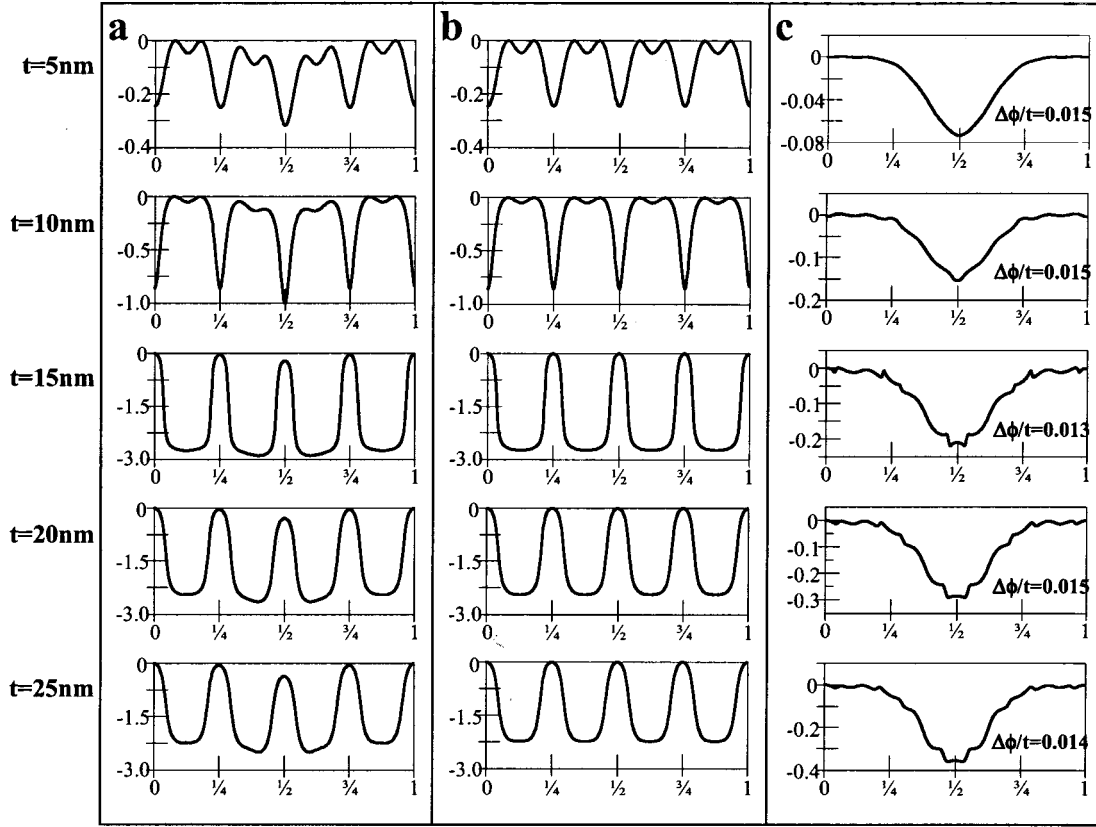


FIG. 3. Dynamical multislice calculation of phase shift (in radians) along the c axis of Bi/2212 unit cell (in fractional coordinates) as a function of sample thickness, (a) with and (b) without 2 V Gaussian GB potential. Full calculation included diffracted beams to 0050; the profiles shown reflect a 6 Å resolution to simulate holography data. (c) Difference profile (representing ϕ_{GB}) between (a) and (b) (i.e., $\phi_{\text{GB}} = \phi_{\text{total}} - \phi_{\text{bulk}}$) scales linearly with thickness indicating “kinematical” treatment of GB is valid.

validity of separating the total phase into GB and bulk contributions, we have performed a number of dynamical calculations.

Figure 3(a) is a series of dynamical multislice calculations of the phase profile expected across a 2 V Gaussian profile twist boundary in Bi/2212 as a function of thickness from 5 to 25 nm. The series in Fig. 3(b) are equivalent calculations with the GB potential omitted, i.e., calculations of $\phi_{\text{bulk}}(x)$. The multislice algorithms and computer code was developed in house, and also used in our earlier publication involving Bi/2212 (001) twist GB's.¹³ The GB supercell consisted of four crystal unit cells on each side of the GB with interfacial plane located between the BiO double layers. Although the model does not consider the out-of-plane atomic relaxations, it agrees extremely well with the HRTEM observations.¹³ The dynamical calculations shown in Figs. 3(a) and 3(b) included scattering up to the 0050 reflection with slice thickness of 0.25 nm, $C_s = 0.55$ mm, and $\Delta f = 0$, but the profiles were calculated with a resolution restricted to 6 Å to simulate profiles obtained from holography experiments. The dynamical scattering strongly affects the phase profiles, but there is effectively no coupling of scattering between the GB and bulk, as shown in Fig. 3(c), where the difference between the total profile [Fig. 3(a)] and the bulk profile [Fig. 3(b)] is shown. Figure 3(c) represents $\phi_{\text{GB}}(x)$ which, furthermore, scales linearly with thickness. This last point means

that not only may the GB phase profile be obtained by a simple subtraction of the bulk contribution, but that the resulting phase profile may be treated “kinematically,” as discussed next, to obtain the GB potential profile.

Since the multislice calculations show that the GB phase scales linearly with thickness, we may write $\phi_{\text{GB}}(x) \approx C_E V_{\text{GB}}(x)t(x)$, where C_E is a constant that depends on the accelerating voltage of the microscope, $V_{\text{GB}}(x)$ is the GB potential and $t(x)$ is the thickness of the sample. This is the kinematical approximation commonly used to determine the projected potential from the reconstructed phase in electron holography. In principle, the thickness may be obtained from the reconstructed amplitude image $A(x)$ as

$$t(x) = -2\lambda \ln A(x), \quad (7)$$

where λ is the mean free path for inelastic scattering.¹⁷ It is essential, however, that the amplitude is reconstructed with the inclusion of all diffraction intensity of the sideband. This is certainly not the situation for our experiments, as clearly evident from Fig. 2(b). To circumvent this problem, we modify Eq. (7) by replacing λ with an effective mean free path λ_{eff} appropriate for Bi/2212 in a systematic row orientation and for amplitude reconstructed to 6 Å resolution. This effective mean free path can be experimentally determined by recording holograms containing significant portions of

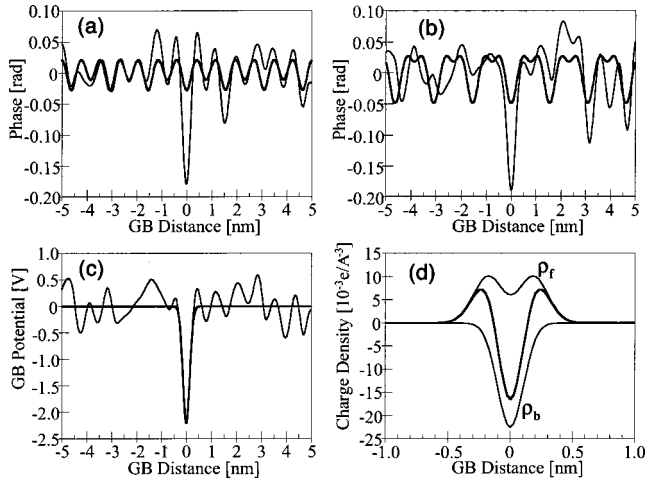


FIG. 4. (a) and (b) Experimental phase profiles (thin lines) reconstructed from different holograms of same GB. Thick lines, representing ϕ_{bulk} , are the result of averaging segments of half-unit cells away from GB. (c) Average GB potential from (a) and (b) after subtraction of ϕ_{bulk} and elimination of thickness dependence ($t = -2\lambda_{\text{eff}} \ln(A)$) from each profile. The thick line is the result of fitting the GB potential to a Gaussian function; the residual variation in the potential away from the GB provides a measure of error. (d) Thick line is the total charge density profile obtained from Poisson's equation applied to the Gaussian fit in (c). The total charge is modeled as the sum of three Gaussians: one representing bound charge (ρ_b) and two symmetrically displaced about the GB representing free charge (ρ_f).

vacuum along with portions of bulk crystal in c -axis row orientation. The holograms were reconstructed as outlined above and the phase was uniquely determined by requiring it to be zero in the vacuum region. From our calculations based on an isolated-atom model, the average potential for Bi/2212 is $V_0 = 19.5$ V, so

$$\lambda_{\text{eff}} \approx \frac{t(x)}{\langle -2 \ln A(x) \rangle} = - \frac{\langle \phi \rangle}{\langle \ln A \rangle} \left(\frac{1}{2C_E V_0} \right), \quad (8)$$

where $\langle \dots \rangle$ denotes a local average over a Bi/2212 unit cell. Experimentally, the local averages $\langle \phi \rangle$ and $\langle A \rangle$ were determined for this measurement by fit of a third order polynomial. The result of Eq. (8) gave $\lambda_{\text{eff}} = 13 \pm 1.3$ nm for these experiments. In subsequent data analysis, then, the sample thickness (taken as constant across the GB) was estimated from the reconstructed amplitude image as $t = -2\lambda_{\text{eff}} \ln(A(\mathbf{r}))$ using $\lambda_{\text{eff}} = 13$ nm.

Figures 4(a)–4(c) illustrates the steps outlined above to extract the interfacial component of the phase and quantify the GB potential. Figures 4(a) and 4(b) are experimental phase profiles (thin line) reconstructed from two separate holograms obtained from the grain boundary depicted in Fig. 2. The profiles are the result of averaging about 20 nm along the interface, and are typical of profiles obtained from the (001) twist boundaries. For each phase profile, partial profiles representing individual unit cells away from the interface were extracted from the data and averaged together to produce an experimentally determined profile appropriate to

the bulk crystal, shown by the thick lines in Figs. 4(a) and 4(b). The resulting bulk profiles were subtracted from each data set, the phase was converted to potential as $V_{\text{GB}} = \phi_{\text{GB}}/C_E t$ and the data sets were averaged together. The result for this GB is shown by the thin line in Fig. 4(c). The variation in the potential profile away from the interface is taken to represent a measure of error in the extracted potential. In this case, the standard deviation away from the boundary in Fig. 4(c) is 0.46 V and is consistent with the estimated measurement sensitivity of 0.3 V discussed above. Corresponding potential profiles were obtained for additional GB's, as discussed in the following section.

IV. MEASUREMENT RESULTS OF GB POTENTIAL AND CHARGE DISTRIBUTION

A. Modeling potential and interface properties

In order to address material properties of the grain boundaries that we have examined, and to facilitate quantitative comparisons, we modeled the GB potential as a Gaussian fit to the experimental profiles. Fitting results for the averaged GB profile are shown in Fig. 4(c) by the thick line. The main advantage of fitting the potential with an analytic function was to simplify interpretation of physical quantities derived from the potential distribution. In particular, the charge density profile obtained from Poisson's equation, which involves a second derivative of the potential, is sensitive to noise fluctuations and residual variations left in the potential profile away from the GB if applied directly to the experimental data. By fitting the potential profile, the charge density may be calculated analytically. Figure 4(d) shows the charge density (thick line) corresponding to the GB in Fig. 4(c) calculated by Poisson's equation

$$\rho(x) = -\epsilon_0 \epsilon_r \nabla^2 V_{\text{fit}}(x), \quad (9)$$

where ϵ_0 is the permittivity of free space and $\epsilon_r = 2.55$ is the calculated relative permittivity of Bi/2212.¹⁸ The charge density profile indicates a negative charge associated with the interface core and compensating positive space charge region.

Additionally, we may consider the extent of nonzero charge density, which defines the width of the GB. We find it reasonable to take the width as the full-width-tenth-minimum of the Gaussian potential fit. In this case, the GB width shown in Fig. 4 is 8.6 Å and is representative of additional GB's summarized below. We note that this value is an upper bound to the GB width due to the 6 Å spatial resolution of our holographic reconstruction. That is to say, a broadening of the measured GB in real space is expected from convolution of the point-spread function associated with the aperture function used to extract the sideband in Fourier space. Nevertheless, our measured width is consistent with prior high-resolution TEM results¹³ where the out-of-plane strain was found to extend less than 10 Å across the GB.

The charge distribution calculated above may, in general, be described as the sum of charge distributions representing charge bound to the interface $\rho_b(x)$ and of unbound (free) charge $\rho_f(x)$ such that $\rho(r) = \rho_b(r) + \rho_f(r)$. For example,

TABLE I. Summary of Bi/2212 [001] twist boundaries.

	Misorientation angle	Potential [V]	Boundary width [Å]	Net bound charge density [e/cell]
GB1	2°	2.06±0.17	9.1	-1.6
GB2	21°	2.31±0.46	7.7	-2.6
GB3	32°	2.20±0.36	8.6	-1.7
GB4	18°	2.38±0.24	8.0	-2.0
Avg.		2.18±0.12	8.6	-1.7

the bound charge term may be due to off-stoichiometric oxygen at the GB, or by reconfiguration of the bonds at the interface, while the free charge may be due to a compensating redistribution of nearby valence electrons or “holes.” For simplicity, we suppose the bound charge has a Gaussian distribution centered at the interface, and that the free charge is the sum of two Gaussians displaced symmetrically from the GB. The result of fitting the charge density in this manner is also shown in Fig. 4(d), where the bound and free charge densities are plotted individually. It is interesting to calculate the total charge associated with the bound charge density. In this case ρ_b corresponds to a total negative charge of about $2e$ per unit cell consistent with, for example, enrichment of 1 oxygen ion per unit cell at the GB. Similar analysis of additional GB’s and more detailed discussion of results are presented next.

B. Summary and discussion of measurements

More than half a dozen twist boundaries were carefully chosen for detailed analysis. As with most of the (001) twist boundaries in Bi/2212, the boundaries were located between the BiO layers and were atomically straight and sharp without apparent grooving as evaluated by HRTEM.¹³ Four pure (001) twist boundaries are summarized in Table I those with Ca/CuO intercalation will be published separately. Portions of holograms from each of the GB’s detailed in Table I, are shown in Fig. 5. The holograms clearly show the interference fringes crucial for reliable amplitude and phase reconstruction. The fringe spacing is about 2 Å in each hologram, and the BiO-BiO layers are clearly resolved indicating the GB is viewed edge on. For each GB, the misorientation angle between the grains was determined from diffraction patterns of the adjacent grains. The angle was defined by the orthorhombic symmetry of Bi/2212, so may range from 0°–90°. For the GB’s detailed here, angles were measured to be 2°, 21°, 32°, and 18°, respectively, for GB1–GB4. GB3 corresponds to the data presented above.

The results of Table I do not show any trend of the measured GB potential on the misorientation angle where the reported error is the standard deviation to the GB potential fit. In fact, the weighted average (by $1/\sigma^2$) of the measured potential for these four GB’s falls within the error bar of each measurement, giving an average potential of 2.18 V with absolute deviation ± 0.12 V. This suggests that electrical properties of these twist boundaries are weakly governed by intrinsic differences directly related to the interfacial geom-

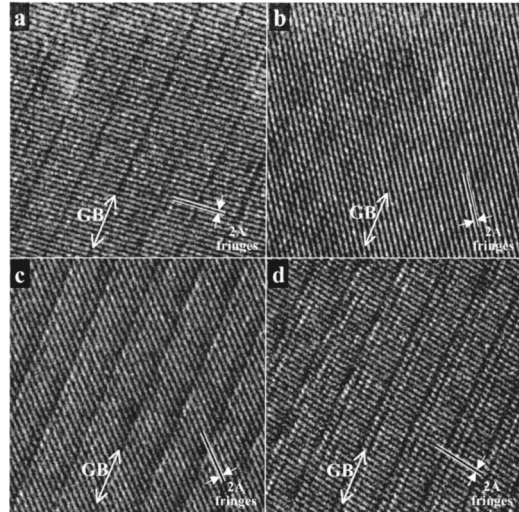


FIG. 5. (a)–(d) Portions of holograms from four GB’s chosen for detailed analysis as summarized in Table I corresponding to GB1–GB4, respectively. In each case, the orientation of the holographic interference fringes is indicated and the GB position is marked. The good interference fringe contrast (about 15–20 %) is critical for reliable amplitude and phase reconstruction.

etry. It is natural, then, to assume that the precise chemical composition including the nature of interfacial defects and average defect density is the most prevailing influence on the electrical activity. Such differences between the GB and grain interior may not be detectable by chemical analysis using EDX and EELS or by dislocation analysis using diffraction contrast for these (001) twist boundaries.¹³ Nevertheless, our measurements indicate that the twist boundary potential appears independent of misorientation angle, which is consistent with measured electrical transport properties of Bi/2212 twist boundaries.¹² If our modeling assumptions about the bound and free charge components of our measured charge profile are correct, these results may also explain why the critical current J_c assumes nearly the same value across the GB as in the grain interior. In particular, our results suggest a net free charge, or accumulation of electron holes, of $+1.7e$ per unit cell near the grain interface. This increased hole concentration, along with the narrow GB width may support incoherent Cooper-pair tunneling to account for the undiminished J_c .¹² Analysis currently underway of similar twist boundaries with adjacent stacking faults consisting of extra or missing Ca/CuO₂ planes in Bi/2212 and examination of GB’s in other high- T_c superconductors such as YBCO may shed additional light on the origin and nature of the GB potentials we have measured. Combined with holography studies of GB’s (Ref. 19) and defect dislocations²⁰ in other materials, a better understanding of interfaces may be gained.

V. CONCLUSIONS

The modeling presented in this study based on off-axis electron holography measurements allows us to address one of the most important physical properties of polycrystalline functional materials: grain boundary potential. The treatment

we have outlined to separate out the bulk contribution at the GB region provides a direct means to measure the potential distribution at interfaces on the nanoscale. We have analyzed the effect of objective lens aberrations and defocus on the quantification of measurements from electron holography, and we have found that they may be neglected for resolutions above about 5 Å for our microscope. This relaxes experimental demands and significantly simplifies quantification. We have applied our treatment to the case of (001) twist boundaries in Bi/2212, where we measure an average GB potential of 2.18 ± 0.12 V independent of grain misorientation at the interface. We further find an average GB width about 8.6 Å, and a negative charge at the core of the interface compensated by positive space charge in its vicinity. These observations may explain the measured transport properties

in Bi/2212 bicrystals and tapes where the dominant grain interconnections are made by (001) twist boundaries. We expect the foundation put forth here to stimulate more comprehensive modeling and additional experiments to further broaden our understanding of interfaces.

ACKNOWLEDGMENTS

We are grateful for the calculations of Haibin Su that contributed to this work, and for useful discussion with Qiang Li over possible interpretations of our results. We are also grateful to Masaki Suenaga for stimulating discussions and for providing the samples used in this study. This work was supported under U.S. DOE Contract No. DE-AC02-98CH10886.

-
- ¹See, for example, A. P. Sutton and R. W. Balluffi, *Interfaces in Crystalline Materials* (Oxford University Press, Oxford, 1995).
- ²D. Dimos, P. Chaudhari, and J. Mannhart, Phys. Rev. Lett. **61**, 219 (1988); Phys. Rev. B **41**, 4038 (1990).
- ³S. E. Babcock, X. Y. Cai, D. L. Kaiser, and D. C. Larbalestier, Nature (London) **347**, 167 (1990).
- ⁴D. C. Larbalestier, S. E. Babcock, X. Y. Cai, M. B. Field, Y. Gao, N. J. Hienig, D. L. Kaiser, K. Merkle, L. K. Williams, and N. Zhang, Physica C **185–189**, 315 (1991).
- ⁵C. B. Eom, A. F. Marshall, Y. Suzuki, B. Boyer, F. R. W. Pease, and T. H. Geballe, Nature (London) **353**, 544 (1990).
- ⁶M. F. Chisholm and S. J. Pennycook, Nature (London) **351**, 47 (1991).
- ⁷J. Mannhart and P. Chaudhari, Phys. Today **54** (11), 48 (2001).
- ⁸G. Hammert, A. Schmehl, R. R. Schulz, B. Goetz, H. Blefeldt, C. W. Schnelder, H. Hilgenkamp, and J. Mannhart, Nature (London) **407**, 162 (2000).
- ⁹J. Mannhart and H. Hilgenkamp, Semicond. Sci. Technol. **10**, 880 (1997).
- ¹⁰*Introduction to Electron Holography*, edited by E. Volkl, L. F. Allard, and D. Joy (Kluwer Academic, New York, 1999).
- ¹¹Y. Zhu, M. Suenaga, and R. L. Sabatini, Appl. Phys. Lett. **65**, 1832 (1994).
- ¹²Q. Li, Y. N. Tsay, M. Suenaga, R. A. Klemm, G. D. Gu, and N. Koshizuka, Phys. Rev. Lett. **83**, 4160 (1999).
- ¹³Y. Zhu, Q. Li, Y. N. Tsay, M. Suenaga, G. D. Gu, and N. Koshizuka, Phys. Rev. B **57**, 8601 (1998).
- ¹⁴M. A. Schofield, Y. Zhu, L. Wu, V. V. Volkov, and M. Malac, JEOL News, *Electron Opt. Instrum.* **36E**, 2 (2001).
- ¹⁵J. Cowley, in *High-Resolution Transmission Electron Microscopy and Associated Techniques*, edited by P. Buseck, J. Cowley, and L. Eyring (Oxford University Press, New York, 1988).
- ¹⁶W. J. de Ruijter and J. K. Weiss, Ultramicroscopy **50**, 269 (1993).
- ¹⁷M. R. McCartney and M. Gajdardziska-Josifovska, Ultramicroscopy **53**, 283 (1994).
- ¹⁸H. Su (unpublished).
- ¹⁹V. Ravikumar, R. P. Rodrigues, and V. P. Dravid, Phys. Rev. Lett. **75**, 4063 (1995).
- ²⁰D. Cherns and C. G. Jiao, Phys. Rev. Lett. **87**, 205504 (2001).